University of California
Los Angeles

A Twin Study using Automated Brain Shape Segmentation Algorithms

A thesis submitted in partial satisfaction
of the requirements for the degree
Master of Science in Statistics

by

Meenakshi Mani

2007

The thesis of Meenakshi Mani is approved.

Yingnian Wu

Jan de Leeuw, Committee Co-chair

Paul M. Thompson, Committee Co-chair

University of California, Los Angeles

2007

To Saraswati . . .

Twirling around in your lotus coracle,

you inspire with your example.

Table of Contents

List of Figures

List of Tables

Acknowledgments

I would first like to thank my thesis advisor, Paul Thompson, for introducing me to the challenges of brain imaging. Paul has not only been very kind to me but he is also the first person I met who spoke enthusiastically about research both in the United States and abroad and I am grateful to him for giving me this international perspective.

I would like to acknowledge the help of Natasha Leporé, Yi-yu Chou and Jan de Leeuw. Natasha got me involved in this project, while Yi-yu helped me with the data processing. The automated segmentation algorithm using multi-atlas fluid registration was developed and implemented by Yi-yu, Natasha, and Paul. Jan de Leeuw showed me how to implement REML by writing a very helpful tutorial. For this, and many other things, I would like to thank each of them.

During the course of my master's work, I got the opportunity to visit INRIA in France. I would like to thank Josiane Zerubia and Xavier Descombes of the Ariana project for inviting me. I am also grateful to Anuj Srivastava, who I met there, for introducing me to statistical shape analysis.

Chapters One through Three are a version of our unpublished paper "Mapping Genetic Influences on Brain Shape using Multi-Atlas Fluid Image Alignment". I would like to acknowledge the contribution of Yi-yu Chou, Natasha Leporé, Agatha Lee, Jan de Leeuw, Katie McMahon, Margie Wright, Arthur Toga and Paul Thompson as co-authors. Figures 1.1 and 2.3 are courtesy of Paul Thompson/UCLA.

Abstract of the Thesis

A Twin Study using Automated Brain Shape Segmentation Algorithms

by

Meenakshi Mani

Master of Science in Statistics

University of California, Los Angeles, 2007

Professor Paul M. Thompson, Co-chair

Professor Jan de Leeuw, Co-chair

In this pilot study, we validated a set of automated surface segmentation shape extraction algorithms to study genetic influences on the brain structure of normal twins. A set of manually delineated lateral ventricles was deformed, using a 3D Navier-Stokes fluid image registration algorithm, onto all the scans in the database of twin brain MRI images. The geometric transformations thus obtained were used to propagate the segmentation labels to all the other brain images. 3D radial distance maps were derived to encode anatomical shape differences. The proportion of shape variance attributable to genetic factors, known as the heritability, was estimated from the shape models using a restricted maximum likelihood formula to increase statistical power. Segmentation errors associated with the projection of labels onto new images were greatly reduced through multi-atlas averaging. The resulting algorithms provide a convenient and sensitive tool to recover and analyze small intra-pair image differences.

In summary, here we show how computer vision approaches based on fluidly

deformable parametric surfaces can be applied to automatically delineate and parameterize brain structures in an image database, and detect genetic influences on brain shape.

CHAPTER 1

Introduction

1.1 Overview

The application of shape analysis to the morphological study of brain structure has garnered much recent interest. Many scientific studies [TCN01, PFL00, LCB06] have reported on overall brain volume inheritance (see Peper et al. [PBB07] for a review). Volume heritability, however, is a non-specific marker. To gain a more complete understanding of the role genetics plays in shaping brain morphology, it would be helpful to identify specific structures and pinpoint locations within them that contain genetic signals. Once identified, the structural features that are most strongly influenced by genes, can in turn, serve as markers for a disease trait, for instance, or to screen and test for effects of specific candidate genes (polymorphic alleles) that are thought to influence brain morphology (such as apolipoprotein E4 [PDQ95], and brain-derived neurotrophic factor (BDNF)).

Shape characterization can detect group differences or changes over time, as well as disease and genetic effects on brain structure. The selection of appropriate shape representations such as Procrustes analysis of a set of 3D anatomical landmarks [Goo91], or medial axis representations [SG01], can be used to quantify shape variation in anatomical structures. A recent twin study [GSS01, SLM05] examined the genetic effects of neurodegenerative disease on lateral ventricles using two surface-based shape measures, one derived from a medial representation

and the other involving spherical harmonics. Medial representations describe the boundary of a closed shape in terms of the distance and angle of boundary points relative to a medial curve or surface threading through the center of the structure, while spherical harmonics provide a complete orthonormal series expansion for closed shapes, and can be used in conjunction with statistical dimension reduction techniques such as principal component analysis to find principal modes of variation. Their findings suggest that shape statistics can uncover group differences that volume measurements are unable to detect.

The lateral ventricles make for an interesting study in shape analysis. These central cavities that serve as conduits for cerebrospinal fluid (CSF) in the brain (see Figure 1.1), exhibit dysmorphic enlargement in a range of neurodevelopmental and neurodegenerative diseases such as Alzheimer's disease, schizophrenia [RRC82] and bipolar illness. Ventricular size and shape are altered as these diseases progress [MSL01]. It is well known that these diseases also have a strong genetic component. Those at heightened genetic risk for schizophrenia (e.g., a patients unaffected twin or sibling) have enlarged ventricles compared to healthy controls [BOH01, SLM05], as do those at genetic risk for Alzheimer's disease [CLZ07a] compared to elderly controls. There is great interest in identifying the anatomical selectivity of these gene effects and, once identified, the specific genes that cause them [CHE05, CTE06].

In this thesis, we use statistical shape analysis to look at the genetic influences on the lateral ventricular structure. Our shape parameter is a radial measure, the perpendicular distance from the medial core to the 3D mesh that constitutes the surface. Using a classical twin design framework, we seek to establish a genetic continuum by looking at degrees of relatedness in various pairings as measured by the intra-class correlation (ICC). To assess heritability, we pool

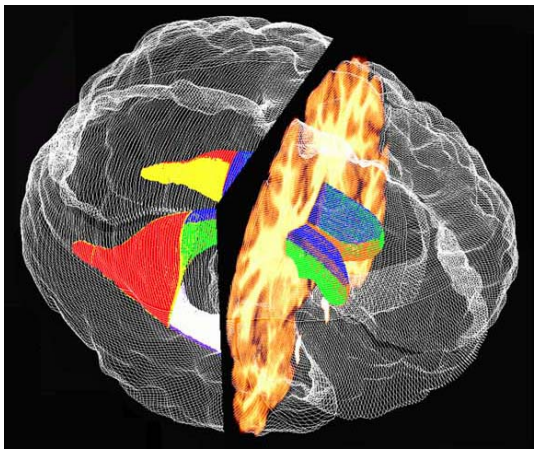

Figure 1.1: **Shape models of the Lateral Ventricles in a Brain MRI Scan.** A set of 3D parametric mesh surfaces is used to represent the lateral ventricles, a fluid-filled structure in the brain. A coronal section from the corresponding 3D MRI scan, and a model of the brain surface (white mesh) are also shown for context. The anterior horns of the ventricles are shown in blue (top surface) and green (bottom surface), and the posterior horns are shown in red (top surface) and yellow (bottom surface).

the data from both monozygotic (identical) and dizygotic (fraternal) twins and solve a restricted maximum likelihood (REML) expression using Fisher's scoring routine. This restricts the number of parameters being estimated, thereby giving us more statistical power for the small sample size (16 pairs). It also enables us to obtain non-negative heritability estimates.

We combine this study with a new automated segmentation procedure developed by Chou et al. [CLZ07a]. There is a compelling reason to adopt automated techniques as the expertise and time required for manual delineation make large-scale clinical studies impractical. We compute a surface model of the ventricular surface based on the medial axis representation, in order to assess shape differences between groups of subjects. The brain images are first put into spatial correspondence using linear affine transformations and then fluidly registered [CRM96] to an individual DZ brain on which the ventricles were manually

segmented. The manual label is propagated to each of the brain images using the displacement fields from the registration step. A multi-atlas averaging technique significantly reduces the random error introduced through automatic label propagation. Since inter-class group studies are sensitive to error and intra-pair studies even more so, minimizing these errors is important in group studies of this nature.

The interaction between genes and environment and their effects on brain structure are still largely unknown as their detection requires automated shape or volume analysis, and computational methods to detect gene effects on structures extracted from populations of 3D images. Ours is one of the first studies to combine genetic modeling with computer vision based algorithms to create a robust automated system that only requires human involvement at the initial stages.

1.2 Thesis Outline

This thesis is organized as follows:

- Chapter 2 is a comprehensive description of the steps required to pre-process the MRI data for genetic analysis. It starts with a brief description of the image acquisition methods followed by rigid and nonrigid registration. The full details of the registration methods used can be found in the Appendix A. Next, automatated surface segmentation is described including the new multiple image registration method, used to improve the accuracy. Finally, the computation of the shape parameter is discussed. The relative merits of all these methods is also briefly discussed.

- Chapter 3 discusses the notion of heritability in quantitative genetics in the

context of the classical twin design. Quantitative measures or statistics of interest such as intraclass correlation (ICC) and heritability, are explained next.

- In Chapter 4 we present the results of the statistical analysis, starting with the raw data, followed by the ICC values and finally the heritability results.
- We conclude with a discussion of the relevance of this work and the directions for future work.

CHAPTER 2

Automated Segmentation of Ventricles and Extraction of the Shape Parameter

2.1 Overview

Computational anatomic studies of large brain MRI databases have led to significant neuroscientific discoveries regarding brain changes throughout life and in disease. Even so, the effects of genetics and environment on brain structure are still largely unknown as their detection requires large image databases, automated shape or volumetric analysis, and computational methods to detect gene effects on structures.

Here we combine several powerful computer vision algorithms with genetic modeling techniques to detect subtle and localized effects of genetic factors on brain structure. In this chapter, we discuss these computer vision approaches, which, collectively describe a surface segmentation shape extraction scheme.

2.1.1 Segmentation

Segmentation is an important image processing step that, in the brain imaging context, separates out cortical structures and regions of interest in a brain image. The segmented brain provides an anatomical framework for functional visualization for applications such as neurosurgical planning and in neuroscience

research. Brain segmentation also serves as a preliminary step for registration, warping, voxel-based morphometry [AF00], and quantitative study. In this work, it is necessary to segment the ventricles to collect shape defining parameters for statistical evaluation.

2.1.2 Automated Segmentation

Automated segmentation and labeling of 3D brain images is a challenging problem. Many structures are complex and variable in shape, making accurate and reproducible segmentation difficult. At the same time, automated approaches are needed for a vast range of medical applications. Many population-based studies of Alzheimer's disease, multiple sclerosis, and schizophrenia [TBH07] now use sequential imaging to examine brain changes over time in hundreds or even thousands of subjects, making automated analysis essential. There is also scientific and commercial interest in identifying treatments, genes, environmental or demographic factors that influence brain integrity, as quantified by computational measures. This discovery is being held back by the lack of algorithms to automatically identify and compare models of brain anatomy on a large scale.

2.1.3 Literature Overview

Many algorithms have been proposed to partially automate brain structure extractions. These still require some amount of expert knowledge and user input such as selecting several points by hand on the structure boundary to initialize a deformable template close to the structure, prior to high-dimensional fluid registration. Hogan et al. [HMW00] used a fluid registration model to deform a template hippocampal surface model into new subjects' scans, yielding a set of models that were analyzed for group differences in shape in Alzheimer's dis-

ease (AD) [ACD03] and shape asymmetries [WGH05]. Level-set or active surface methods, which use partial differential equations to evolve a deforming template under image-derived forces, often require some interactive initialization for accurate label propagation [YPH06].

Some groups have attempted fully automated subcortical segmentation, such as [CMH07] and [FSB02], who used a Markov Random Field model to encode statistical prior information on the expected intensities and adjacencies of structures. Zhou et al. [ZR05] used fuzzy templates to automatically segment different brain structures based on information extracted from a set of training images. Artificial neural networks were used by Ferrarini et al. [FPO06] to study ventricular shape variations in healthy elderly and AD subjects, generating a control average surface and a cloud of corresponding nodes across a data set. Heckemann et al. [HHA06] performed label propagation using free-form deformations and decision fusion to provide automated anatomical segmentations of the brain.

Multi-atlas methods have also been proposed to address the problems of error introduced through the automation process. These are described in [DHT99, FSB02, HHA06, SMH05].

2.1.4 Our Approach

In this study, we fit a surface model of the ventricles based on the medial axis representation, and use it to assess shape differences in a population of subjects. The brain images are first registered through global affine transformations and then fluidly registered [CRM96] to an individual subject's brain on which the ventricles have been manually segmented. This manual label is propagated to each of the brain images using the displacement fields from the registration step. The procedure is performed on a set of three reference brains, whose labelings

are then combined by averaging. Finally, the radial distance to the medial axis is computed. The details of this procedure can be found in [CLZ07a, CLZ07b].

The multi-atlas averaging technique dramatically reduces random error introduced through automatic label propagation from a single reference image. Furthermore, this approach eliminates the problem of disconnected voxels that are commonly found in other bottom-up segmentation methods that independently classify each individual voxel as belonging to the structure or not, based on a feature set.

The steps, from the acquisition of the MRI data to the extraction of the quantitative shape parameter (see Figure 2.1) are described below.

2.2 Image Acquisition

Magnetic Resonance(MR) is the brain imaging technology of choice for neuroscientific studies because it allows one to tailor the image to the anatomic part of interest and to the disease process being studied. The desired imaging effects can be acheived by adjusting a set of intrinsic parameters. Adjusting the T1 and T2 spin relaxation times, for instance, allows one to acheive the right contrast to highlight a feature. A good reference that covers MRI principles in detail is [LL99]. Because MRI data is stored as a 3D digital image, it can pre-processed and analyzed using image processing methods.

2.3 Rigid Registration

The first of these pre-processing steps is rigid registration. In order to segment anatomical brain structures using the multi-atlas method, the brain images first

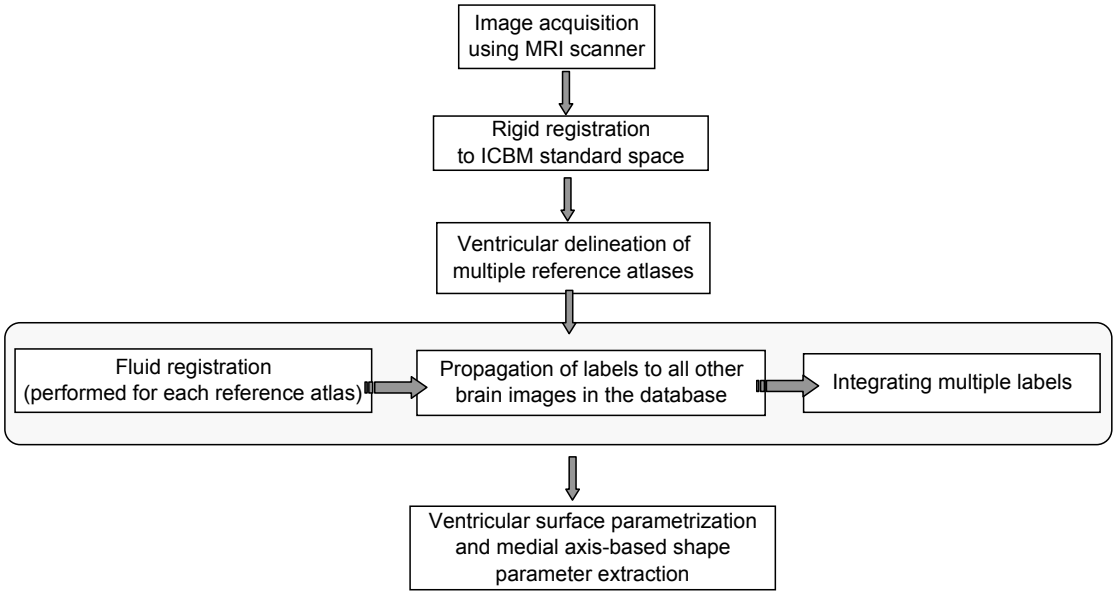

Figure 2.1: Data Pre-processing Path

need to be put into spatial correspondence. We use global linear transformations (translations, rotations and scalings) to spatially normalize the images as a first step to exact alignment.

2.4 Expert Ventricular Delineation

A set of brain scans are randomly selected from the twin brain MRI database and the lateral ventricles are manually traced in consecutive coronal slices. For this study, we used three atlases as references. The accurate identification of neuroanatomic boundaries was facilitated by the MultiTracer [Woo03] application

software.

2.5 Fluid Registration

The fluid registration approach we follow, first described by Christensen [CRM96], treats the deforming image as a compressible viscous fluid whose motion is governed by the nonlinear Navier-Stokes partial differential equation (PDE)

$$\mu\nabla^2\mathbf{v} + (\mu + \lambda)\nabla(\nabla \cdot \mathbf{v}) + b(\mathbf{x}, \mathbf{u}) = 0. \tag{2.1}$$

For constant force, this expression is linear and is a key step in the numerical solution of the PDE. A 3D convolution filter in a multiresolution grid [BG96, GB97] serves as a linear operator and is used to solve this equation. The force that drives the deformation is derived from a similarity based cost function. In this case, an intensity matching function was used because ventricular CSF has high contrast. Registration procedures are described in greater detail in Appendix A.

Our approach addresses some of the challenges presented by the automatic segmentation of lateral ventricles and similar anatomical structures. First, the fluid model ensures the deformation mappings are diffeomorphic, i.e., formally guaranteed to remain one-to-one to match homologous anatomical points. Second, deformable templates can fit a model through what can be partially disconnected sets of CSF voxels in the regions where the lateral ventricles are thin or indeterminate.

2.6 Propagation of Contours using a Single Atlas

The geometric transformations that map the source to the target during non-linear registration are diffeomorphic, i.e., smooth one-to-one mappings. We can therefore perform an inverse transform to map landmarks on the target to homologous points on the source. Using trilinear interpolation, a 3D contour of the shape is constructed, which when propagated to the unlabelled images in the database, results in the automatic segmentation of the lateral ventricle or other anatomical brain structure.

2.7 Multi-Atlas Alignment

There are errors inherent in an automatic labelling procedure. Systematic errors may arise due to a bias in the registration process or in the expert labelling while random errors occur from fine tuning the individual registrations. As a result, label propagation is dependant on the choice of the target image with different targets resulting in different segmentations.

To improve label propagation accuracy, we manually delineate and label 3 targets. Each of these targets is used to independently segment the brain images in the database resulting in each image being assigned three sets of labels. These labels are then fused into one through linear averaging.

Chou et al. [CLZ07a, CLZ07b] have shown that increasing the number of labeled atlases, N, resulted in an asymptotic decrease in the average error between manually and automatically extracted models. In their case, the labeling error, measured using the symmetrized Hausdorff distance (see Appendix C), was averaged over 16 lateral ventricles and plotted after each of 9 targets was added. They found that only 3-4 reference atlases were needed to realize the full potential of

this averaging method. It is thought that this averaging procedure significantly reduces the effects of random digitization errors from the manual segmentations. The resulting average model is somewhat robust to inaccuracies in individual registrations, which may occur when non-global minima of the intensity-based cost function are reached.

The combination of segmentations is not a new idea, but, it has not been previously applied and validated for surface-based segmentations. This method does not require any operator input other than the initial expert labeling of a small set of images.

2.8 Ventricular Shape Metrics

In order to use statistical shape analysis to identify regional differences in ventricular morphology, we first extract the shape parameter from the shape model. This is a surface-based shape measure which combines surface mesh modeling [THZ04, TSL96, TST96] with medial axis shape representation. Points representing the contours of the lateral ventricles previously segmented as described above, are resampled so that a regular parametric grid is mapped onto the surface. The medial axis, which curves through the cross-sectional centroids of the 3D shape to form the backbone, is the reference from which the (perpendicular) distance to the grid points at the surface is measured (see Figure 2.3). These radial distances, evaluated at each of the mesh nodes, allow statistical comparisons of local surface contractions and expansions at homologous surface locations across subjects to be made. Local shape differences between groups or within a group can thus be assessed.

For this study, we evaluated the left lateral ventricle, tracing out the ante-

rior and posterior horn. Data from the inferior horn was not used because it is not a consistent feature in young healthy subjects. To further increase resolution, we divided these two horns into 2 sections, top and bottom. Sets of points representing the tissue boundaries from each region were resampled and made spatially uniform by stretching a regular parametric grid ($100 \times 150 = 15,000$ surface points) over each surface. The number of left ventricular locations sampled ($15,000 \times 4 = 60,000$ points) gives us a sensitive tool to detect shape differences between the groups.

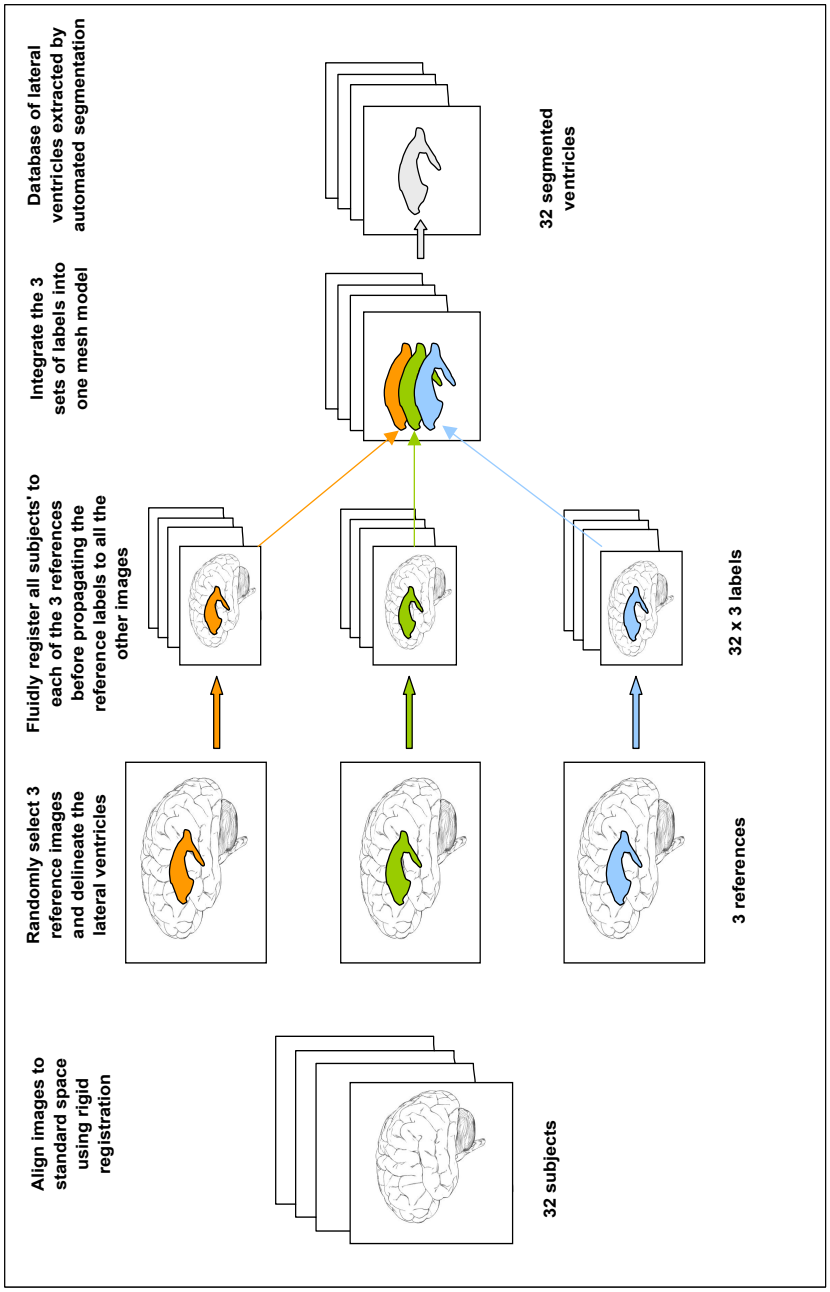

Figure 2.2: Multi-Atlas Fluid Image Alignment.

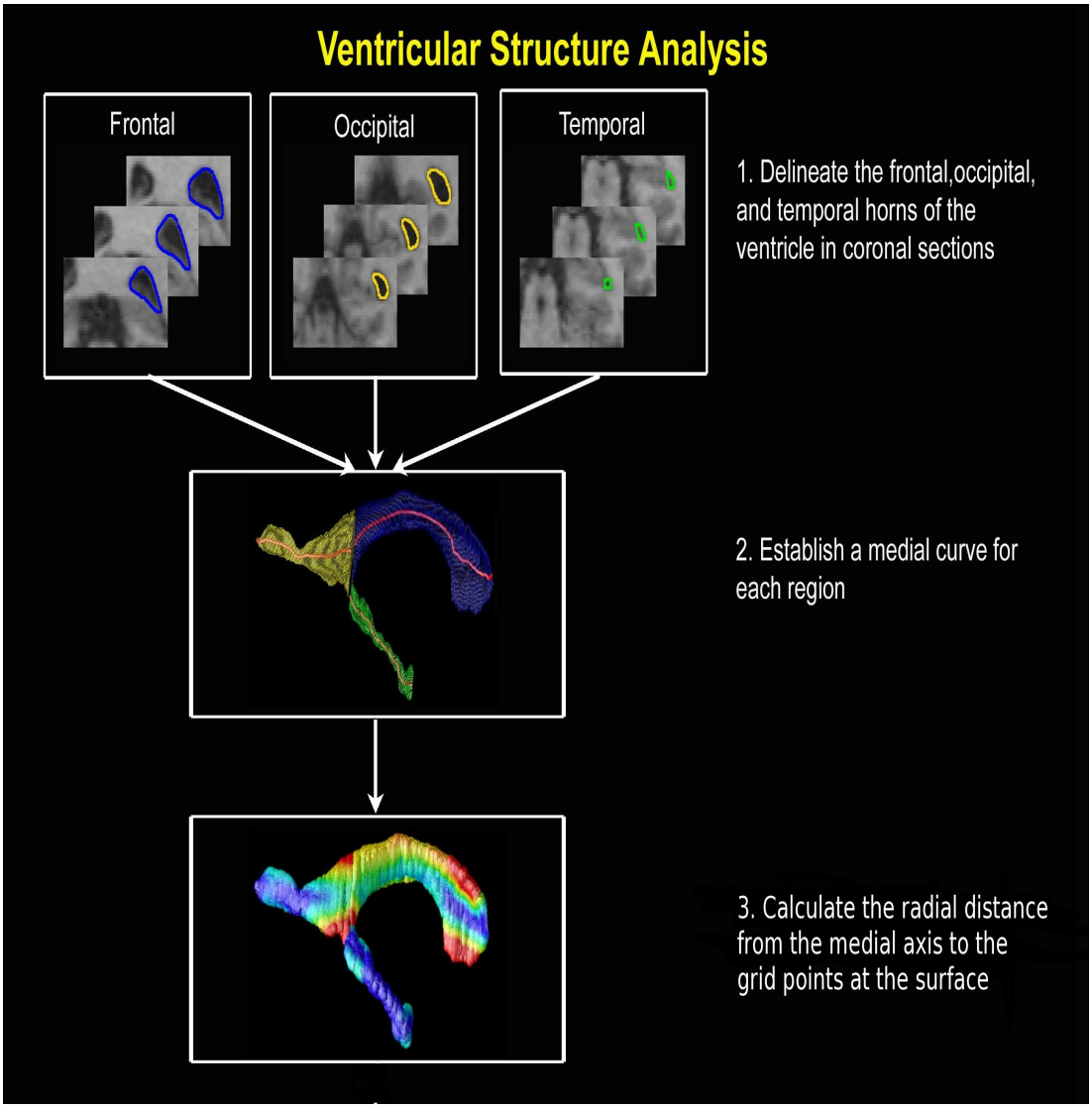

Figure 2.3: A flow chart to show how ventricular distance maps are computed.

CHAPTER 3

Concepts from Quantitative Genetics

A phenotype is a specific biological trait such as eye color, that can be measured in a population; such a trait is typically influenced by genes and the environment. Heritability is the proportion of phenotypic variance attributable to genetic variance. It ranges in value from 0.0 (where genes do not contribute at all to individual phenotypic differences) to 1.0 (individual differences are entirely attributable to genetic differences). Heritability also depends on the range of typical environments in the population studied. If the environment of the population is fairly uniform, as in the case of twins reared together, heritability can be estimated from phenotypic measures in identical and fraternal twins, as each type of twin differs in genetic similarity.

3.1 Classical Twin Design

The twin design provides a mechanism to study the relative contribution of genes to phenotypic variability. Monozygotic (MZ) twins are genetically identical, while fraternal or dizygotic (DZ) twins share, on average, 50% of their genes. By extending comparisons to pairs with varying degrees of kinship, we design a genetic continuum from which to assess heritability of brain substructure.

3.2 Intraclass Correlation Calculation

The standard approach to measure the degree of relationship for twin or other unordered data pairs is to use the intraclass correlation (ICC). The analysis of variance (ANOVA) formulation (cf. Appendix D),

$$r = \frac{MS_{between} - MS_{within}}{MS_{between} + MS_{within}} \tag{3.1}$$

treats each pair as a random effect and the data from the members of each pair are viewed as measurement errors; this model is widely used in twin study calculations.

Due to the variability inherent in estimates derived from a small sample, the computed ICC values may be negative. We can correct this to get non-negative ICC values, usually by increasing the sample size. This can be explained by the fact that the $MS_{between}$ and the MS_{within} are estimates of the population variance σ^2, but the $MS_{between}$ is calculated from sample means and the MS_{within} is calculated from sample variances. Adding more twin pairs to the study will not affect the within-pair variance, but it will affect the distribution of the means if there are differences between twin pairs. The net affect is for the estimated ICC to become positive as additional twin pairs are included.

For this study, we use the restricted maximum likelihood (REML) method, which gives an unbiased ICC estimate [Lee07]. The non-negative REML formula is given by

$$r = \max\left(0,\ \frac{\frac{n}{n-1}MS_{between} - MS_{within}}{\frac{n}{n-1}MS_{between} + MS_{within}}\right) \tag{3.2}$$

where n is the number of twin pairs.

3.3 Heritability Calculation

The simplest expression for heritability is

$$h^2 = \frac{r}{G}, \tag{3.3}$$

where G is the degree of genetic similarity (assumed to be 0.5 for DZ and 1.0 for MZ twins) and r is the ICC. From this, we can obtain independent estimates of heritability from either group of twins. Heritability may also be estimated by combining information from both sets of twins using Falconer's formulation [Fal81]

$$h^2 = 2(r_{MZ} - r_{DZ}). \tag{3.4}$$

Since the number of pairs is small, we specify a more restrictive likelihood model with a smaller number of parameters. We do this by pooling the MZ and DZ data. We assume that both groups are distributed with the same mean, μ, and variance, σ^2, and that they differ only by their covariances, ω^2_{MZ} and ω^2_{DZ}. The negative log-likelihood $L(\mu, \sigma^2, \omega^2_{MZ}, \omega^2_{DZ})$ must be minimized over $\sigma^2 > \omega^2_{MZ} > \omega^2_{DZ}$ using an iterative algorithm. This ensures that the heritability estimates are non-negative. We compute initial values from method of moments estimates and use Fisher's scoring algorithm given by:

$$\mathbf{\Theta}_{i+1} = \mathbf{\Theta}_i + I(\Theta)^{-1} V(\Theta) \tag{3.5}$$

where i is the iteration step size, I is the Fisher information and $V(\Theta)$ is the score function. This is an alternative to the Newton-Raphson method where the Hessian is replaced by the expected value of the Hessian.

CHAPTER 4

Statistical Shape Analysis

In this chapter, the statistical analysis of the left lateral ventricular data of healthy twins is discussed. The statistical evaluation is divided into three parts: analysis of raw data, analysis of ICC, heritability results.

4.1 Subjects

3D anatomical brain imaging data was acquired from 32 subjects, 10 MZ (6 males, 4 females) and 6 same-sex DZ (4 males, 2 female) twin pairs, as part of a 5-year research study of 700 pairs of twins. Informed consent was obtained from all participants and the study was approved by the institutional review boards at UCLA and the University of Queensland. The subjects ranged in age from 22-25 years and all were healthy. Zygosity was established objectively by typing nine independent DNA microsatellite polymorphisms (PIC > 0.7) by using standard polymerase chain reaction (PCR) methods and genotyping. These results were crossed checked with blood group (ABO, MNS, and Rh), and phenotypic data (hair, skin and eye color), giving an overall probability of correct zygosity assignment of greater than 99.99%.

4.2 MRI Image Acquisition and Pre-processing

3D T1-weighted images were acquired from all subjects on a 4 Tesla Bruker Medspec whole body scanner, located at the CMR and Wesley Hospital MRI Research Facility in Queensland, Australia. Subjects were scanned using a customized MP-RAGE 3D T1-weighted sequence to resolve anatomy at high resolution (0.9 mm isotropic resolution); TR=2500 ms; TE=3.83 ms; T1=1500 ms; pulse angle=15; coronal orientation; FOV $230 \times 230 \times 230$ mm^3 ; the acquisition matrix was $256 \times 256 \times 256$. All the images were spatially normalized to the International Consortium for Brain Mapping (ICBM-53) average brain imaging template [CNP94] using 9 parameter registration (i.e., 3 rotations, 3 translations, 3 scalings).

4.3 Data

The raw data is a set of radial measures from each of the 4 sections of the left lateral ventricle: top anterior, bottom anterior, top posterior, bottom posterior. The radial distance is the length from the medial core to a grid point on the 3D surface. An intraclass correlation (ICC) statistic and heritability coefficient was computed at each of the $15,000$ surface grid points. A total of $15,000 \times 4 = 60,000$ lateral ventricular locations were sampled.

4.4 Exploratory Analysis of Raw Data

We first plotted histograms (see Figure 4.1) of the radial measures. These distributions reflect the shape of the structure. The right skewed distributions we see indicate the presence of small peripheral regions. This also demonstrates the

ability of a deformable template based segmentation technique to included and connect the peripheral regions.

Summary statistics for each section and for the ventricle as a whole are shown in Tables 4.2 and 4.3. The mean and median values for MZ twins are less than the corresponding values for DZ twins. This is most obvious in the anterior regions. The null hypothesis that the two groups of twins come from the same distribution was tested using two non-parametric tests, the Kolmogorov-Smirnov test and the Wilcoxon rank sum test. The differences were found to be significant (p-value $\ll 0.00001$). Although our findings are contrary to the assumptions of the twin design that the distributions have the same mean, it has been suggested that MZ twins are in fact smaller on many anthropological characters and that this may have to do with shared chorion or placenta [DDS82]. It should be pointed out that some of the other published studies looking at ventricular volume between twins found no significant differences [].

The effects of multi-atlas labeling are evident when Tables 4.2 and 4.3 are compared. Table 4.3 gives a summary of data that resulted from the averaging 3 reference templates. Since the averaging results in higher means and the distribution shift is significant (p-value $\ll 0.00001$), it suggests that the ventricle delineated through averaging is larger than one where a single ventricle reference is used.

4.5 Intraclass correlations

ICC values computed at 60,000 mesh points of the ventricular surface were used to construct ICC maps for MZ and DZ twins (see Figure 4.2). These ICC values are also summarized (mean and standard deviation) in Table 4.4. The intra-

class correlation coefficients were numerically greater in identical twins than in randomly selected non-related pairs of subjects, for all of the measures chosen. Although quantitative testing of the differences in correlations for identical versus fraternal twins would require a large sample to confirm, this pilot sample shows that ICCs are numerically greater for twins with greater genetic affinity. Evidence for a genetic continuum alone, in which similarity is greatest for MZ twins, somewhat less for DZ twins, and negligibly small for randomly selected unrelated subjects, does not mean genetic influences are dominant. MZ twins should also have correlations that are at least twice that of DZ twins.

The effects of multi-atlas segmentation and labeling of the images is also evident from Table 4.4. When 3 ventricular templates are propagated into each brain scan and averaged, the net effect, relative to using a single template, is to reduce a source of methodological error, namely the error associated with labeling of the ventricles. Because this source of labeling error is diminished, Table 4.5 shows that in general all the ICC coefficients increase for every measure chosen, and for each type of twin. This is reasonable, as the sources of labeling error include hand digitization errors in the templates, as well as minor errors in boundary correspondence due to imperfect fluid image registration. Because the magnitude of these errors is not likely to be correlated between members of a twin pair (or an unrelated pair), their removal results in all the ICCs increasing.

4.6 Heritability

Heritability values were computed using a REML scoring algorithm and are plotted in Figure 4.5. The values range from 0.0 (since we constrained the values to be non-negative) to 1.2 (due to the variance in a small sample, we can expect values to be greater than 1.0). The mean values, tabulated in Table 4.1 range

	1 Atlas		3 Atlases	
	Mean	SD	Mean	SD
Top Anterior	0.17	0.28	0.11	0.22
Bot Anterior	0.15	0.32	0.08	0.19
Top Posterior	0.16	0.22	0.10	0.17
Bot Posterior	0.19	0.26	0.07	0.14

Table 4.1: Heritability summary for 1 and 3 Atlases: h^2(1 Atlas) > h^2(3 Atlas averaging).

from 0.15 to 0.19 for the 4 sections indicating that environmental variance is the dominant influence. These values are lower than LV volume heritability reported in previous studies. From Figure 4.5 and Table 4.1, we can also see that multi-atlas averaging had a marked effect on the heritability, consistently lowering the estimate for all four venticular sections. The ICC trends seen in Figure 4.4 may explain this. With multi-atlas averaging, both ICC_{MZ} and ICC_{DZ} increase, but ICC_{DZ} increases by a greater percentage. The heritability, which is computed from their difference, can therefore be expected to decrease.

4.6.1 Heritability Distribution

A non-parametric distribution of heritability values gives us the uncorrected p-values. Figure 4.7 shows the uncorrected and corrected p-values for the Top Anterior section. (The plots for the other 3 sections are similar). From the p-map we see that there is no genetic signal. A distribution for the heritability was computed which allows for minimal distributional assumptions. The heritability values are not significant and corrections for multiple comparisons (FDR or FWER) were not necessary.

	MZ(n=10)		DZ(n=6)	
	Mean	SD	Mean	SD
Top Anterior	4.959	2.255	5.266	2.275
Bot Anterior	4.939	2.112	5.298	2.150
Anterior	4.949	2.185	5.282	2.213
Top Posterior	5.446	2.905	5.469	2.821
Bot Posterior	5.299	2.717	5.227	2.688
Posterior	5.373	2.814	5.348	2.758
Total	5.161	2.528	5.315	2.501

Table 4.2: Radial distance(mm) measured using 1 atlas.

	MZ(n=10)		DZ(n=6)	
	Mean	SD	Mean	SD
Top Anterior	5.330	2.200	5.710	2.244
Bot Anterior	5.729	2.097	6.188	2.132
Anterior	5.529	2.159	5.949	2.202
Top Posterior	5.401	3.106	5.399	3.003
Bot Posterior	5.296	2.903	5.241	2.845
Posterior	5.349	3.007	5.320	2.926
Total	5.439	2.619	5.634	2.608

Table 4.3: Radial distance(mm) measured using 3 atlases.

4.6.2 Discussion

The cumulative evidence from these tests, the low heritability values, the fact that these scores are lowered further when the source of methodological error is reduced and the high pvalues obtained, suggest that the shape variation in lateral ventricles is largely influenced by environmental factors. The ICC_{DZ}, in particular after atlas averaging, is more than half the MZ correlation (see Figure 4.4), suggesting the influence of shared environmental factors.

	MZ (n = 10)		DZ (n = 6)		NR (n = 10)	
	Mean	SD	Mean	SD	Mean	SD
Top Anterior	0.35	0.20	0.23	0.26	0.11	0.15
Bot Anterior	0.38	0.21	0.20	0.22	0.07	0.11
Top Posterior	0.42	0.22	0.25	0.22	0.03	0.11
Bot Posterior	0.46	0.23	0.21	0.21	0.05	0.10

Table 4.4: ICC using 1 Atlas: $ICC_{MZ} > ICC_{DZ} \gg ICC_{NR}$.

	MZ(n=10)		DZ(n=6)		NR(n=10)	
	Mean	SD	Mean	SD	Mean	SD
Top Anterior	0.37	0.22	0.27	0.26	0.15	0.18
Bot Anterior	0.39	0.24	0.26	0.23	0.10	0.13
Top Posterior	0.51	0.19	0.32	0.28	0.02	0.04
Bot Posterior	0.58	0.20	0.30	0.26	0.05	0.10

Table 4.5: ICC using 3 Atlases: $ICC_{MZ} > ICC_{DZ} \gg ICC_{NR}$.

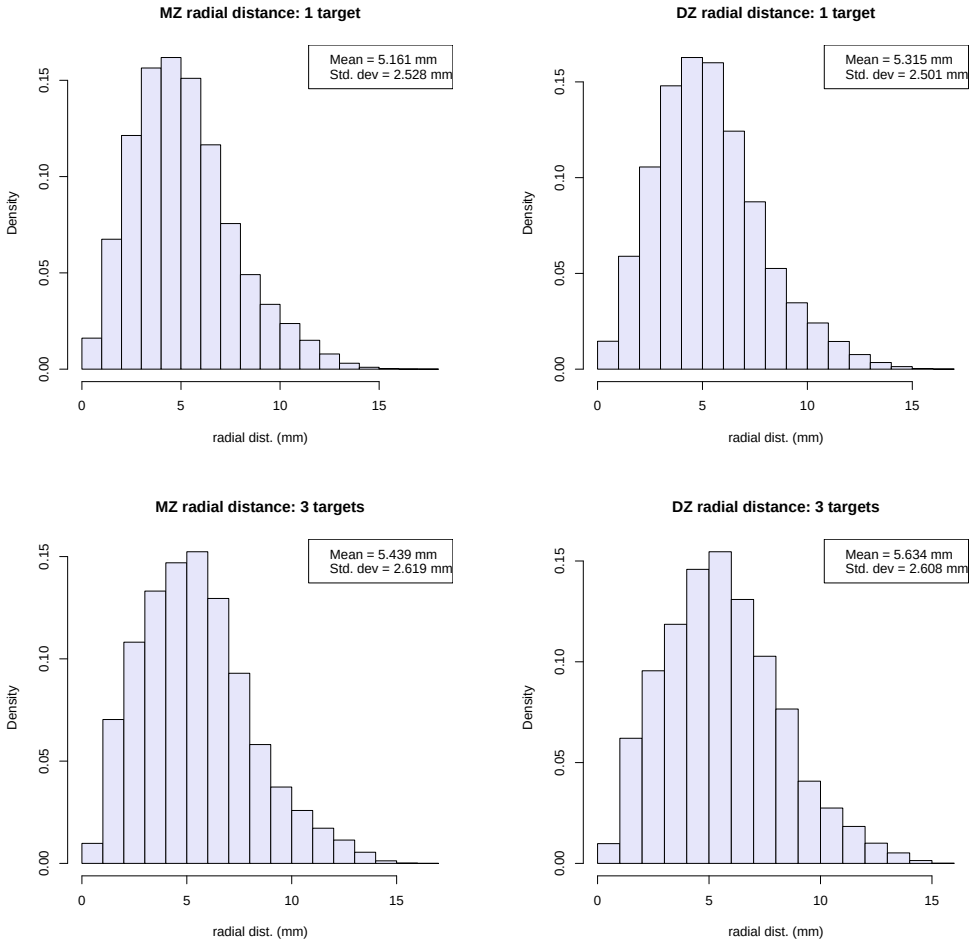

Figure 4.1: Histograms of radial distance for MZ and DZ twins. Top: registered using 1 atlas; Bottom: registered using 3 atlases.

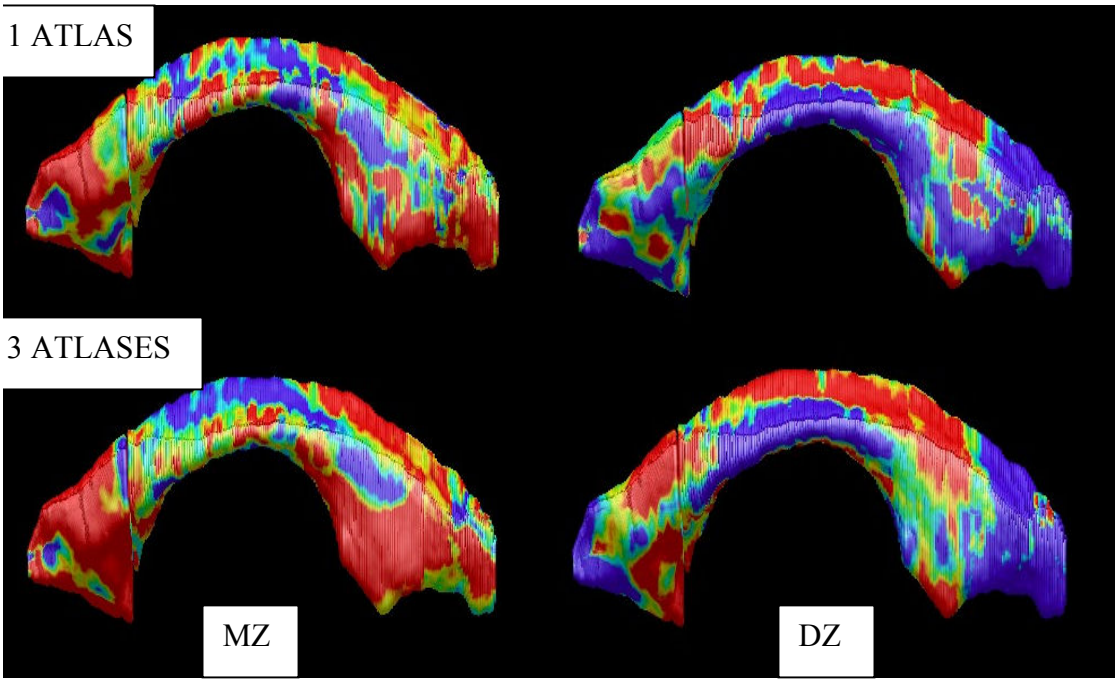

Figure 4.2: Intraclass correlation maps. Genetically similar MZ twins (left) have greater intra-pair similarity than do DZ twins (right). These similarities increase as the number of reference atlases increase (bottom left, MZ; bottom right, DZ), suggesting that a source of error has been reduced. The increase in ICC values is indicated by the increased presence of red ($r > 0.5$).

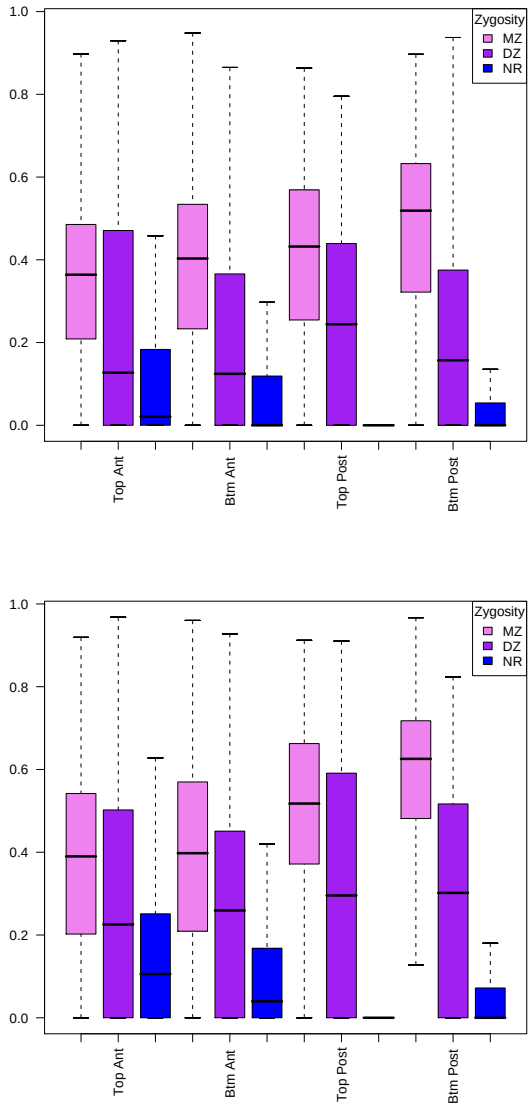

Figure 4.3: Boxplots comparing ICC values for MZ, DZ and NR pairs for 1 atlas(top) and 3 atlases (bottom). For the Top Anterior, Bottom Anterior, Top Posterior and Bottom Posterior locations of the lateral ventricle, $ICC_{MZ} > ICC_{DZ} \gg ICC_{NR}$. The null hypothesis that there is no significant difference between the means for any given pairing was rejected in all cases.

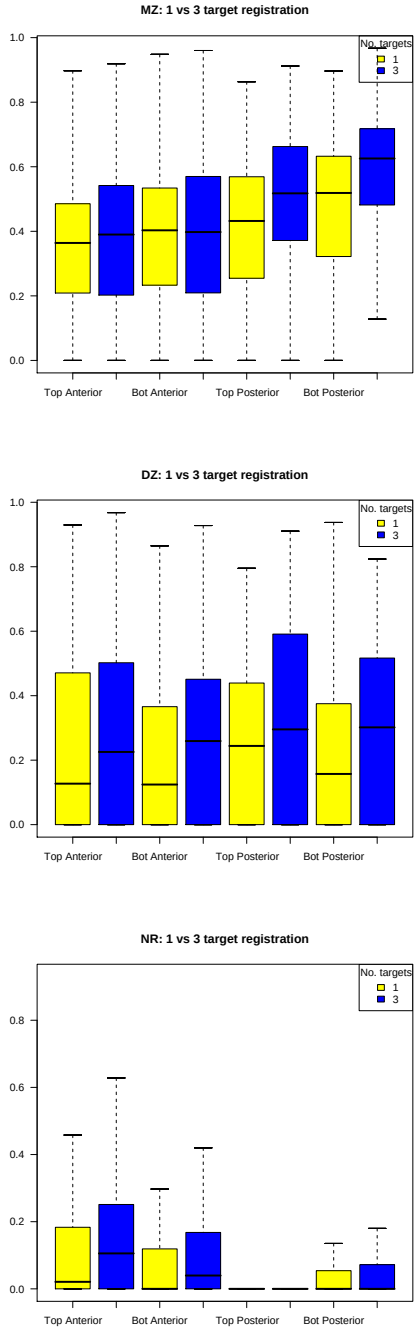

Figure 4.4: ICC values for 1 and 3 atlas averaging for MZ (top); DZ (center); NR (bottom); Here we compare the ICCs for measures derived from anatomical segmentations that use a single deformable surface template, versus the generally more accurate segmentations derived from averaging the results of three deformable surface segmentations. The higher ICCs obtainable with more templates suggest that the anatomical labeling error has been reduced and would otherwise be a major source of methodological error, depleting power to assess genetically influenced shape differences

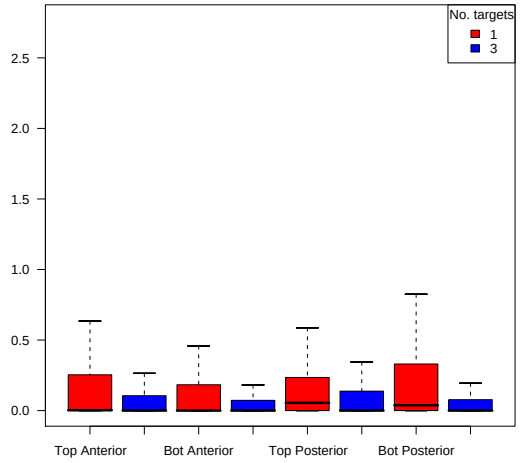

Figure 4.5: Heritability is low and decreases further after 3 target averaging.

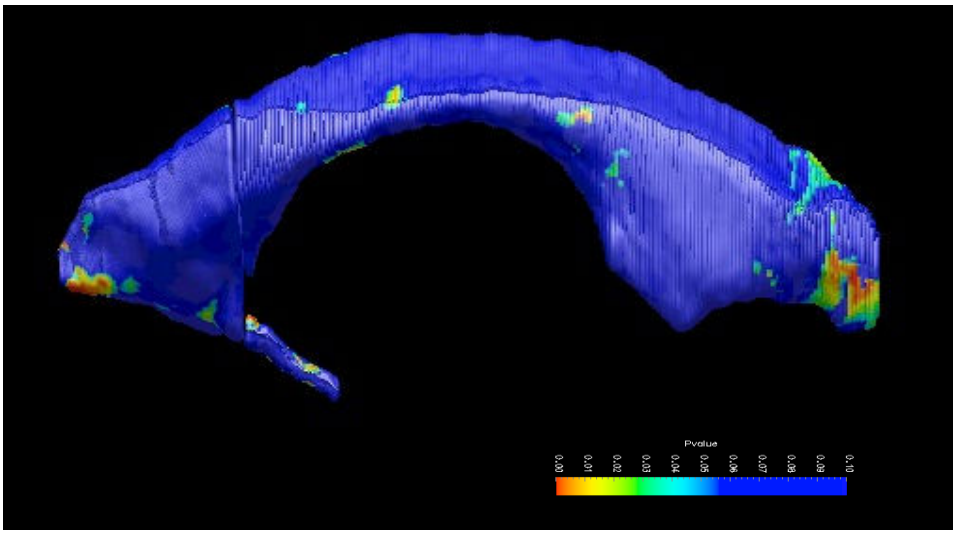

Figure 4.6: Heritability p-value map. The p-values, computed by generating a non-parametric distribution, were not significant as evidenced by the large blue areas on the map. ($p > 0.05$).

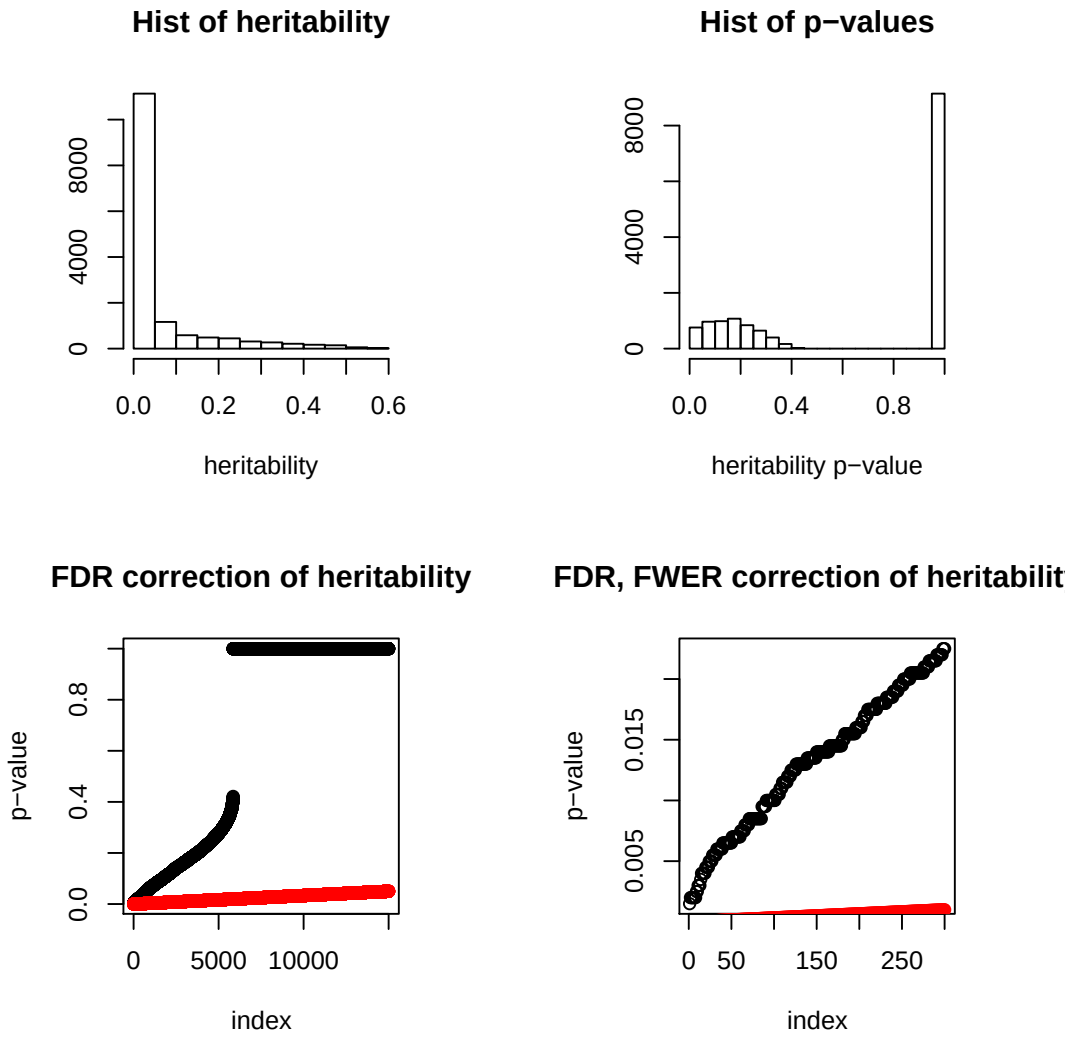

Figure 4.7: Heritability p-values: The histogram for heritabililty (top left) shows most values are between 0 and 0.1. A histogram for the p-values obtained from a non-parametric distribtion and not corrected for multiple comparisons, show most are not significant (top right). No signal was obtained after FDR and FWER corrections were applied to the p-values (bottom left and right).

CHAPTER 5

Discussion

In this study, we combined algorithms for automated brain image segmentation, fluid image registration, surface parameterization, shape statistics and quantitative genetics in a novel way to automatically assess how genes influence brain structure in a medical image database. We performed fluid segmentation of the lateral ventricles using a 3D Navier-Stokes registration model in an MRI database of twins, modeling surface shape variation using surface-based statistics derived from a medial axis transform. The segmentation approach is novel as it uses multi-template averaging and a hybrid surface- and volume-based high-dimensional image registration to improve accuracy. In initial studies, some other groups [GSS01, SLM05] have proposed approaches for modeling genetic influences on brain shape and volume in twins. Here we use a stable and robust restricted maximum likelihood method to compute genetic effects on brain structure, as well as proportions of variance attributable to genes, including tests of reliability (via the use of different anatomic templates for labeling) and estimates of heritability computed in an expanding MRI database.

Even in this pilot study, which is intended to provide a proof of concept for the approach, this benefit of multi-atlas versus single-atlas image segmentation is substantial, with ICCs for identical twins rising from 0.4 to 0.5 in some cases with the addition of multiple segmentation templates (or atlases; see Tables 1 and 2). This increased genetic signal-to-noise ratio may be of substantial value if these

image-derived measures are to serve as a quantitative endophenotype to search for the effects of individual candidate genes on brain structure, as the database is expanded.

APPENDIX A

Image Registration

In order to perform a statistical evaluation of inter-subject anatomical brain differences, the brain images first need to be put into spatial correspondence. The images are typically aligned to a given reference such that each anatomical point or landmark in the image is matched to a homologous point in the reference. This process of aligning two images by mathematically deforming one to coincide with the other using a best-fit similarity criteria is called image registration. Registration approaches can be classified as rigid or nonrigid. They differ based on the image acquisition methods used and the kind of study to be performed.

A.1 Rigid Registration

Rigid registration is characterized by simple rotations and translations. These transformations are global in nature and preserve internal distances and angles. Rigid registration is commonly applied in situations where there is little change in brain shape or position within the skull. It is thus suitable for cases where the image data for a single subject is acquired over a short period of time often with different imaging modalities such as CT, MRI or PET. Affine registration, an extension of rigid registration which includes shears and scale adjustments, expands the scope of applications. Since it can be described compactly requiring just somewhere between 6 to 12 parameters (i.e. upto 3 rotations, 3 translations,

3 shears, 3 scalings) it is typically used as a first approximation to full nonrigid registration (see Figure A.1) or for the interpolation of missing features.

A.2 Nonrigid Registration

Affine mappings can only approximate the complex transformations required to put two brain images into correspondence. To completely transform a source image to the target image we need to apply nonlinear deformations locally to correct for the discrepancies (see Figure A.1). These spatial deformations are driven by external forces which minimize image differences as quantified by similarity measures. The image itself is treated as a physical entity–an elastic solid or a viscous fluid–to which a force is applied. The physical motivation underlying the nonrigid matching problem is reflected in the mathematics which is an amalgam of elastic theory and fluid dynamics.

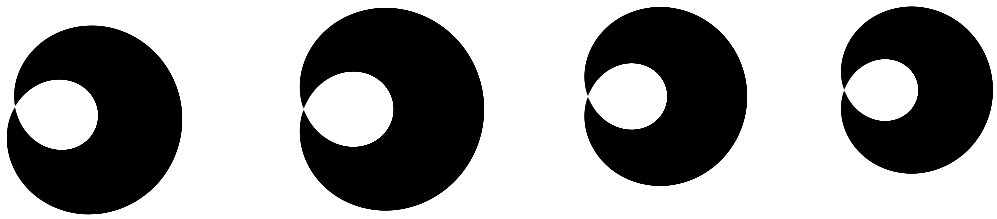

Source image Rotation Scaling Target image

Figure A.1: Transforming the source to the target through rigid, affine and nonrigid deformation.

A.2.1 The Variational Framework

The conceptual basis for nonrigid registration is the optimization of the objective function [GB99]

$$\text{cost} = \text{deformation} - \text{similarity}.$$

The similarity is some measure of the difference in image intensities between the two templates. The deformation term, introduced to account for noise in the image or in cases where the image data is missing, is a penalty that is imposed to ensure smoothness. The similarity term, from which the deformation forces are derived, can be thought of as a potential function. Extending the mechanical analogy, the cost function can be likened to an expression of Hooke's law with the similarity being the stress and the deformation being the strain.

The similarity measure can be optimized by minimizing $\int \|I_{source} - I_{target}\|^2$ in a least squares fit. Energy is the integral of the potential so in keeping with the physical analogy, this integral is the potential energy. The deformation offsets the similarity term till equilibrium is reached and the total potential energy of the system, the cost function, is minimized. Because the image matching problem is described in variational terms, powerful numerical techniques exist to solve the equations.

A.2.2 The Elastic Model

Broit and Bajcsy [Bro81, BB82], were the first to model the source image as an incompressible elastic solid that deforms to match a canonical reference known as an atlas. To drive the elastic-matching process, they introduced this variational physics-based formulation for 3D registration of the brain. Bajcsy and Kovačič [BK89] subsequently implemented a more efficient procedure that guides the reg-

istration in a nested fashion from coarse to fine resolution. Corrections made at the coarser stages are propagated so that smaller adjustments are required at the finer resolutions. This multiresolution scheme lowers the computational costs. The success of the 3D elastically deformable model has since spawned a body of literature – some of these efforts have reformulated the problem in decision theoretic terms using Bayesian modeling [Gee99, GB99]. Of particular relevance to the development of the viscous model (cf. Section A.0.3.3) is the work of Amit, Grenander et al. [AGP91] and Miller, Christensen et al [MCA93] who derive the driving force based on a Gaussian sensor likelihood in place of the correlation based similarity measure employed by Bajcsy.

Limitations of Elastic Registration Elastic registration is not a general purpose application. Its use is restricted to small deformations where the internal strains generated do not exceed the elastic bounds. Moreover, the use of a quadratic penalty function limits the size of the deformation. This prevents complete registration when the deformations are large.

A.2.3 The Fluid Model

To accomodate the large and complex deformations involved in inter-subject brain registration, Christensen [CRM96] proposed a viscous fluid model based on the theory of fluid dynamics. Here the source template, T, is modeled as a viscous fluid that flows out to match the reference, R. A local force is applied to the template in a direction that gives the best fit to a second image. This deforming force is thus defined by the characteristics of the target image.

Eulerian Frame of Reference In fluid registration, position is referenced in Eulerian coordinates as opposed to the Lagrangian coordinates used in elastic registration. An Eulerian reference frame is fixed in space and does not track of the movement of individual particles. Rather, location is described in terms of the final position: a particle at position $\mathbf{x}$ at time t in the template image, originated at position $\mathbf{x} - \mathbf{u}(\mathbf{x}, t)$ at time t_0. Here $\mathbf{u}(\mathbf{x}, t)$ is the displacement of the particle as it moves through $\mathbf{x}$. This method of accounting is more efficient than the Lagrangian approach where a particle is parameterized with the initial position as a reference. When a material deforms, the Lagrangian grid deforms with it and can sometimes overlap and contort. The use of Lagrangian coordinates is thus only suitable for the small cohesive deformations characteristic of elastic registration. The Eulerian reference, in contrast, allows for the relaxation of internal stresses that build up in response to the deformation. Large deformations are thus possible.

In the Eulerian frame, the velocity field is defined as

$$\mathbf{v}(\mathbf{x}, t) = \nabla \mathbf{u}(\mathbf{x}, t)\mathbf{v}(\mathbf{x}, t) + \frac{\partial \mathbf{u}(\mathbf{x}, t)}{\partial t}. \tag{A.1}$$

This is obtained by the application of the chain rule of differentiation (cf. Appendix B).

Navier Stokes PDE This framework allows the motion of the fluid to be described in terms of the Navier-Stokes partial differential equation (PDE)

$$\mu \nabla^2 \mathbf{v} + (\mu + \lambda)\nabla(\nabla \cdot \mathbf{v}) + b(\mathbf{x}, \mathbf{u}) = 0. \tag{A.2}$$

The Laplacian, $\nabla^2 = \nabla^T \nabla$, constrains the velocity field. $\nabla^2 \mathbf{v}$ thus represents the viscous flow of fluid. The $\nabla(\nabla \cdot \mathbf{v})$ term allows for growth and shrinkage of the local regions of the template. These two terms represent internal forces that are in equilibrium with the external driving body force. The multiplicative factors, μ and λ are called Lamé parameters and give a convenient representation for Hooke's law. μ is the shear modulus while λ, a combination of other elastic constants, is equivalent to the bulk modulus for fluids. The incorporation of these material constants which capture the features of the underlying elastic body, help maintain a natural deformation process.

The driving force, $\mathbf{b}$, is derived from a Gaussian sensor likelihood function

$$C(T(\mathbf{x}), R\mathbf{u}(\mathbf{x}, t)) = \frac{\mu}{2} \int_\Omega | \left(T(\mathbf{x} - \mathbf{u}(\mathbf{x}, t)) - R(\mathbf{x})\right) |^2 d\mathbf{x}.$$

The variation of this cost function with respect to the displacement field yields the body force

$$\mathbf{b}(\mathbf{x}, u(\mathbf{x}, t)) = -\mu \left(T(\mathbf{x} - \mathbf{u}(\mathbf{x}, t)) - R(\mathbf{x})\right) \nabla T|_{\mathbf{x}-\mathbf{u}(\mathbf{x},t)}. \tag{A.3}$$

In this expression, ∇T is a gradient which determines the direction of the deformation at $\mathbf{x} - \mathbf{u}(\mathbf{x}, t)$. $(T(\mathbf{x} - \mathbf{u}(\mathbf{x}, t)) - R(\mathbf{x}))$, the difference in intensity between the deformed template and the target, is a scalar that weights the gradient. When the two images are perfectly aligned, this term is zero and the deformations cease.

Numerical Solution The viscous PDE given by equations (A.1), (A.2) and (A.3) includes nonlinearities associated with the material derivative and the body force. These nonlinear equations can be solved numerically by decomposing the PDE into a series of linear equations that solve for the velocity field, $\mathbf{v}(\mathbf{x}, t)$, at

each instance of time. These individual steps are then integrated using Euler integration of the material derivative.

Algorithm for fluid registration

1. Initialize $t = 0$ and $\mathbf{u}(\mathbf{x}, 0) = 0$.
2. Calculate the body force $\mathbf{b}$.
3. If $\mathbf{b}$ is below a threshold or the maximum number of iterations is reached, STOP.
4. Solve the (linear) PDE for the instantaneous velocity field, $\mathbf{v}(\mathbf{x}, t)$.
5. Calculate the displacement field using explicit Euler integration of the velocity.
6. Increment t and go to Step 2.

The key step in this algorithm is the solution of the PDE

$$\mu\nabla^2\mathbf{v} + (\mu + \lambda)\nabla(\nabla \cdot \mathbf{v}) + b(\mathbf{x}, \mathbf{u}) = 0.$$

For constant force this PDE is linear and the expression can be rewritten using a linear operator $\mathcal{L}$ that works on $\mathbf{v}$

$$\mathcal{L}\mathbf{v} + b(\mathbf{x}, \mathbf{u}) = 0.$$

Here, $\mathcal{L}\mathbf{v} = \mu\nabla^2\mathbf{v} + (\mu + \lambda)\nabla(\nabla \cdot \mathbf{v})$ has the same form as the linear elasticity operator in Hooke's law. Christensen used a successive over relaxation (SOR) scheme to solve this linear equation but this method is computationally expensive. Bro-Nielson and Gramkow [BG96, GB97] proposed a method that speeds up the algorithm by at least an order of magnitude. Their approach was to use a convolution filter in a multiresolution grid since linear behavior can be modeled by convolution filtering [RK04]. The filter kernel approximates the impulse response

of the deformation media and can thus be used to determine the instantaneous velocity field at each point. The total velocity field can then be obtained by the superposition of the responses for all the forces.

Discussion Fluid registration is a powerful technique. In principle, it is possible to warp any template to any reference but this flexibility also increases the possibility for misregistration.

APPENDIX B

Chain rule for differentiation

To differentiate a composite function $\mathbf{v}(\mathbf{w}(t))$, we apply the chain rule

$$\mathbf{v}(\mathbf{w}(t)) = \frac{d\mathbf{u}(\mathbf{w}(t))}{dt} = \nabla\mathbf{u}\left(\mathbf{w}(t)\right)\nabla\mathbf{w}(t).$$

When $\mathbf{w}(t) = \begin{pmatrix}\mathbf{x}(t) & t\end{pmatrix}^T, \quad \nabla\mathbf{w}(t) = \begin{pmatrix}\nabla\mathbf{x}(t) & I\end{pmatrix}$.

$\mathbf{v}(\mathbf{w}(t))$ can then be written as

$$\begin{aligned}\mathbf{v}(\mathbf{w}(t)) &= \nabla\mathbf{u}\left(\mathbf{w}(t)\right)\nabla\mathbf{w}(t) = \begin{pmatrix}\nabla\mathbf{x}(t) & I\end{pmatrix}\begin{pmatrix}\nabla_x\mathbf{u}(\mathbf{x}(t),t)\\ \nabla_t\mathbf{u}(\mathbf{x}(t),t)\end{pmatrix}\\ &= \nabla\mathbf{u}(\mathbf{x},t)\nabla\mathbf{x}(t) + \frac{\partial\mathbf{u}(\mathbf{x},t)}{\partial t}.\end{aligned}$$

APPENDIX C

Symmetric Hausdorff distance

The Hausdorff distance, $h(A, B)$ between two surfaces A and B is given by:

$$h(A, B) = \max_{a \in A} \min_{b \in B} \|a - b\|_2, \tag{C.1}$$

where $\|.\|_2$ is the L_2 distance. In general, $h(A, B) \neq h(B, A)$. The symmetrized Hausdorff distance

$$h_{sym}(A, B) = \frac{1}{2}\{h(A, B) + h(B, A)\} \tag{C.2}$$

more accurately measures the error between two surfaces, since a distance computed relative to a single surface may underestimate or overestimate the true error.

APPENDIX D

An ANOVA estimate for Intraclass Correlation

Correlations are commonly computed using the standard Pearson product-moment procedure. This involves assigning one member of a bivariate pair to the X variable and the other member of the pair to the Y variable. This designation can be readily made, for instance, with husband-wife data, where each member of the pair unequivocally belongs to a separate category. With twin data however, the characterization of either member of the pair as X or Y is arbitrary. Many $X-Y$ labellings are possible and as a consequence the correlation value obtained is not unique. Consider for example the number of permutations possible with the 3 unordered pairs $(a,b),(c,d),(e,f)$:

X	ace	ade	acf	adf	bcf	bde	bdf	bce
Y	bdf	bcf	bde	bce	ade	acf	ace	adf

8 different $X-Y$ pairings are possible and from these 8 (in actuality, there are 4 since correlation is symmetric about $X-Y$ and half the pairings are mirror images), values for the correlation coefficient can be calculated. More generally, for n unordered pairs, there are 2^n such pairings and these permutations give rise to a distribution of correlation coefficients.

While it is possible to calculate the mean and confidence limits for this distribution and hence infer a value for the correlation, permutation and resampling methods are computationally intensive. A more standard approach for obtaining

a measure for the correlation in situations where we are dealing with unordered pairs is to set up the problem as an analysis of variance (ANOVA) calculation. It is easy to see that if both members of a pair have relatively high values, the mean value for that pair will also be relatively high. Conversely, when both members of a pair have relatively low values, the mean for that pair will be relatively low. Hence, the greater the correlation, the greater will be the variability between the means of the pairs as a proportion of total variability, and the smaller will be the proportion of total variability that exists within the pairs. The degree of relationship can thus be estimated by the proportion of the total variability that is accounted for by between class variance. To distinguish this measure from the Pearson product-moment correlation, we define it as an *intraclass correlation (ICC)* coefficient

$$\rho = \frac{\sigma_s^2}{\sigma_s^2 + \sigma_e^2}. \tag{D.1}$$

In this formulation, σ_s^2 is the true variance between pairs and σ_e^2 is the pooled variance within the pairs. In order to obtain estimates of these parameters, Equation (D.1) can be cast in an ANOVA framework and σ_s^2 and σ_e^2 reinterpreted in terms of the *mean square*. The mean square in ANOVA parlance is an estimate of population variance based on the variability among a set of measures. σ_e^2 is then simply the mean-square estimate of within-pair variance (MS_{within}) computed in ANOVA. If a group or pair is comprised of k members, then the mean-square estimate of between-pair variance ($MS_{between}$) equals k times σ_s^2, the true component, plus σ_e^2, the within pair error component. This is due to the fact that the individual variances add-up and each mean contains a true component and

an error term. In other words,

$$\begin{aligned} MS_{within} &= \sigma_e^2 \\ MS_{between} &= k\sigma_s^2 + \sigma_e^2 \end{aligned}$$

From this we get:

$$\sigma_s^2 = \frac{MS_{between} - MS_{within}}{k}$$

Substituting these in the expression for ICC we have:

$$\begin{aligned} \rho &= \frac{(MS_{between} - MS_{within})/k}{(MS_{between} - MS_{within})/k + MS_{within}} \\ &= \frac{MS_{between} - MS_{within}}{MS_{between} - MS_{within} + kMS_{within}} \\ &= \frac{MS_{between} - MS_{within}}{MS_{between} + (k-1)MS_{within}} \end{aligned}$$

This is the same expression derived by Shrout and Fleiss [SF79] for a design that corresponds to a one-way ANOVA where each pair is a random effect and the members of each pair are viewed as measurement errors. For twin pairs, $k = 2$, and we get the following expression for ICC:

$$ICC = \frac{MS_{between} - MS_{within}}{MS_{between} + MS_{within}} \tag{D.2}$$

The intraclass correlation ranges from 1.0 to -1.0. It is large and postive when there is little variation within the pairs but the means between the pairs differ. It is large and negative when the variation within a pair is much greater than that between the pairs.

References

[ACD03] J. Ashburner, J. Csernansky, C. Davatzikos, N.C. Fox, G. Frisoni, and P.M. Thompson. "Computer-Assisted Imaging to Assess Brain Structure in Healthy and Diseased Brains." *Lancet Neurology*, **2**(2), February 2003.

[AF00] J. Ashburner and K.J. Friston. "Voxel-Based Morphometry – The Methods." *NeuroImage*, **11**:805–821, 2000.

[AGP91] Y. Amit, U. Grenander, and M. Piccioni. "Structural Image Restoration Through Deformable Templates." *Journal of the American Statistical Association*, **86**(414):376–387, June 1991.

[BB82] R.K. Bajcsy and C. Broit. "Matching of Deformed Images." In *ICPR82*, pp. 351–353, 1982.

[BG96] M. Bro-Nielsen and C. Gramkow. "Fast Fluid Registration of Medical Images." In Karl Heinz Höhne and Ron Kikinis, editors, *VBC*, volume 1131 of *Lecture Notes in Computer Science*, pp. 267–276. Springer, 1996.

[BK89] R. Bajcsy and S. Kovačič. "Multiresolution elastic matching." *Computer Vision, Graphics, and Image Processing*, **46**(1):1–21, 1989.

[BOH01] W. F. C. Baaré, C. J. van Oel, H. E. Hulshoff Pol, H. G. Schnack, S. Durston, M. M. Sitskoorn, and R. S. Kahn. "Volumes of Brain Structures in Twins Discordant for Schizophrenia." *Arch Gen Psychiatry*, **58**(1):33–40, 2001.

[Bro81] C. Broit. *Optimal Registration of Deformed Images*. PhD thesis, Universitiy of Pennsylvania, 1981.

[CHE05] T.D. Cannon, W. Hennah, T.G.M. van Erp, P.M. Thompson, J. Lonnqvist, M. Huttunen, T. Gasperoni, Tuulio-Henriksson, T. Pirkola, A.W. Toga, J. Kaprio, J.C. Mazziotta, and L. Peltonen. " DISC1/TRAX Haplotypes Associate with Schizophrenia, Reduced Prefrontal Gray Matter, and Impaired Short- and Long-Term Memory." *Archives of General Psychiatry*, **62**(11):1205–13, November 2005.

[CLZ07a] Y.Y. Chou, N. Leporé, G.I. de Zubicaray, S.E. Rose, O.T. Carmichael, J.T. Becker, A.W. Toga, and P.M. Thompson. "Automated 3D Map-

ping and Shape Analysis of the Lateral Ventricles via Fluid Registration of Multiple Surface Based Atlases." In *ISBI*, 2007.

[CLZ07b] Y.Y. Chou, N. Leporé, G.I. de Zubicaray, S.E. Rose, O.T. Carmichael, J.T. Becker, A.W. Toga, and P.M. Thompson. "Automated 3D Mapping and Shape Analysis of the Lateral Ventricles via Fluid Registration of Multiple Surface Based Atlases." *NeuroImage*, 2007. submitted.

[CMH07] M. Chupin, R. Mukuna-Bantumbakulud, D. Hasboun, E. Bardinet, S. Baillet, S. Kinkingnehun, L. Lemieux, B. Dubois, and L. Garner. " Anatomically constrained region deformation for the automated segmentation of the hippocampus and the amygdala: Method and validation on controls and patients with Alzheimer's disease." *NeuroImage*, **34**:996–1019, 2007.

[CNP94] D. L. Collins, P. Neelin, T. M. Peters, and A. C. Evans. "Automatic 3D intersubject registration of MR volumetric data in standardized Talairach space." *Journal of Comput Assist Tomogr*, **18**(2):192–205, 1994.

[CRM96] G. E. Christensen, R. D. Rabbitt, and M. I. Miller. "Deformable templates using large deformation kinematics." *IEEE Transactions on Image Processing*, **5**(10):1435–1447, 1996.

[CTE06] T.D. Cannon, P.M. Thompson, T.G.M. van Erp, M. Huttunen, J. Lonnqvist, J. Kaprio, and A.W. Toga. "Mapping Heritability and Molecular Genetic Associations with Cortical Features Using Probabilistic Brain Atlases: Methods and Initial Applications to Schizophrenia." *Neuroinformatics*, **4**(1):5–19, 2006.

[DDS82] E. Dupae, E. Defrise-Gussenhoven, and C. Susanne. "Genetic and environmental influences on body measurements of Belgian Twins." *Acta Geneticae Medicae et Gemellologiae*, **31**(3-4):139–144, 1982.

[DHT99] B.M. Dawant, S.L. Hartmann, J.P. Thirion, D. Vandermeulen, and P. Demaerel. "Automatic 3-D segmentation of internal structures of the head in MR images using a combination of similarity and free-form transformations: Part I, methodology and validation on normal subjects." *IEEE Transactions on Medical Imaging*, **18**:909–916, 1999.

[Fal81] D. S. Falconer. *Introduction to Quantitative Genetics*. Longman, second edition, 1981.

[FPO06] L. Ferrarini, W.M. Palm, H. Olofsen, M.A. Buchem, J. H.C. Reiber, and F. Admiraal-Behloul. "Shape differences of the brain ventricles in Alzheimer's disease." *NeuroImage*, **32**(3):1060–1069, 2006.

[FSB02] B. Fischl, D.H. Salat, E. Busa, M. Albert, M. Dieterich, C. Haselgrove, A. van der Kouwe, R. Killiany, D. Kennedy, S. Klaveness, A. Montillo, N. Makris, N. Rosen, and A.M. Dale. "Whole brain segmentation: automated labeling of neuroanatomical structures in the human brain." *Neuron*, **33**(3):341–355, 2002.

[GB97] C. Gramkow and M. Bro-Nielsen. "Comparison of Three Filters in the Solution of the Navier-Stokes Equation in Registration." In *Proceedings of the Scandinavian Conference on Image Analysis-SCIA'97*, pp. 795–802, 1997.

[GB99] J. C. Gee and R. Bajcsy. "Elastic matching: continuum mechanical and probabilistic analysis." In A.W. Toga, editor, *Brain Warping*, pp. 183–197. Academic Press, 1999.

[Gee99] J. C. Gee. "On matching brain volumes." *Pattern Recognition*, **32**(1):99–111, 1999.

[Goo91] C. Goodall. "Procrustes Methods in the Statistical Analysis of Shape." *Journal of the Royal Statistical Society, Series B*, **53**(2):285–339, 1991.

[GSS01] G. Gerig, M. Styner, M. E. Shenton, and J. A. Lieberman. "Shape versus Size: Improved Understanding of the Morphology of Brain Structures." In *MICCAI*, pp. 24–32, 2001.

[HHA06] R. A. Heckemann, J.V. Hajnal, P. Aljabar, D. Rueckert, and A. Hammers. "Automatic anatomical brain MRI segmentation combining label propagation and decision fusion." *NeuroImage*, pp. 115–126, July 2006.

[HMW00] R.E. Hogan, K.E. DSc. Mark, L. Wang, S. Joshi, M.I. Miller, and R.D. Bucholz. "Mesial Temporal Sclerosis and temporal lobe epilepsy: MR imaging deformation-based segmentation of the hippocampus in five patients." *Radiology*, **216**:291–297, 2000.

[LCB06] N. Lepore, Y. Chou, C. Brun, M. Mani, G. de Zubicaray, K. McMahon, and P.M. Thompson. "Genetic Influences on Brain Structure and Fiber Architecture Mapped using Diffusion Tensor Imaging and Tensor-Based Morphometry in Twins." In *Proc. Organization for Human Brain Mapping*, June 2006.

[Lee07] J. de Leeuw. "Variance Components for Sibgroups." Preprint, April 2007.

[LL99] Z. Liang and P. C. Lauterbur. *Principles of Magnetic Resonance Imaging: A Signal Processing Perspective*. Wiley-IEEE Press, October 1999.

[MCA93] M. Miller, G. Christensen, Y. Amit, and U. Grenander. "Mathematical textbook of deformable neuroanatomies." *Proceedings of the National Academy of Sciences*, **90**(24):11944–11948, 1993.

[MSL01] D.H. Mathalon, E. V. Sullivan, K. O. Lim, and A. Pfefferbaum. "Progressive Brain Volume Changes and the Clinical Course of Schizophrenia in Men: A Longitudinal Magnetic Resonance Imaging Study." *Arch Gen Psychiatry*, **58**(2):148–157, 2001.

[PBB07] J. S. Peper, R. M. Brouwer, D. I. Boomsma, R. S. Kahn, and H. E. Hulshoff Pol. "Genetic influences on human brain structure: A review of brain imaging studies in twins." *Human Brain Mapping*, **28**(6):464–473, 2007.

[PDQ95] J. Poirier, M. C. Delisle, R. Quirion, I. Aubert, M. Farlow, D. Lahiri, S. Hui, P. Bertrand, J. Nalbantoglu, B. M. Gilfix, and S. Gauthier. "Apolipoprotein E4 allele as a predictor of cholinergic deficits and treatment outcome in Alzheimer disease." *Proceedings of the National Academy of Sciences*, **92**(26):12260–12264, 1995.

[PFL00] B. F. Pennington, P. A. Filipek, D. Lefly, N. Chhabildas, D. N. Kennedy, J. H. Simon, C. M. Filley, A. Galaburda, and J. C. DeFries. "A Twin MRI Study of Size Variations in the Human Brain." *Journal of Cognitive Neuroscience*, **12**(1):223–232, 2000.

[RK04] P. Rogelj and S. Kovačič. "Spatial Deformation Models for Non-Rigid Image Registration." In Danijel Skočaj, editor, *Proceedings of the 9th Computer Vision Winter Workshop (CVWW'04), Piran, Slovenia.*, pp. 79–88. Slovenian Pattern Recognition Society, 2004.

[RRC82] A.M. Reveley, M.A. Reveley, C. Clifford, and R.M. Murray. "Cerebral ventricular size in twins discordant for schizophrenia." *Lancet*, **540**(I), 1982.

[SF79] P. E. Shrout and J.L. Fleiss. "Intraclass Correlations: Uses in Assessing Rater Reliability." *Psychological Bulletin*, **86**(2):420–428, 1979.

[SG01] M. Styner and G. Gerig. "Medial models incorporating shape variability.", 2001.

[SLM05] M. Styner, J. A. Lieberman, R. K. McClure, D. R. Weinberger, D. W. Jones, and G. Gerig. "Morphometric analysis of lateral ventricles in schizophrenia and healthy controls regarding genetic and disease-specific factors." *Proceedings of the National Academy of Sciences*, **102**(13):4872–4877, 2005.

[SMH05] C. Svarer, K. Madsen, S. G. Hasselbalch, L. H. Pinborg, S. Haugbøl, Vibe G. Frøkjær, S. Holm, O. B. Paulson, and G. M. Knudsen. "MR-based automatic delineation of volume of interest in human brain PET imaging using probability maps." *NeuroImage*, **24**(4):969–979, February 2005.

[TBH07] P.M. Thompson, G. Bartzokis, K.M. Hayashi, A.D. Klunder, P.H. Lu, N. Edwards, M.S. Hong, M. Yu, J.A. Geaga, A.W. Toga, C. Charles, D.O. Perkins, J. McEvoy, R.M. Hamer, M. Tohen, G.D. Tollefson, and J.A Lieberman. "Time-Lapse Mapping Reveals Different Disease Trajectories in Schizophrenia depending on Antipsychotic Treatment." *Journal of Neuroscience*, 2007. submitted.

[TCN01] P.M. Thompson, T.D. Cannon, K.L. Narr, T. van Erp, M. Khaledy, V.P. Poutanen, M. Huttunen, J. Lnnqvist, C.G. Standertskjld-Nordenstam, J. Kaprio, R. Dail, C.I. Zoumalan, and A.W. Toga. " Genetic Influences on Brain Structure." *Nature Neuroscience*, **4**(12):1253–1258, December 2001.

[THZ04] P.M. Thompson, K.M. Hayashi, G.I. de Zubicaray, A.L. Janke, S.E. Rose, J. Semple, M.S. Hong, D. Herman, D. Gravano, D.M. Doddrell, and A.W. Toga. "Mapping hippocampal and ventricular change in Alzheimer's disease." *NeuroImage*, **22**(4):1754–1756, August 2004.

[TSL96] P.M. Thompson, C. Schwartz, R.T. Lin, A.A. Khan, and A.W. Toga. "Three-dimensional statistical analysis of sulcal variability in the human brain." *Journal of Neuroscience*, **16**:4261–4274, 1996.

[TST96] P.M. Thompson, C. Schwartz, and A.W Toga. "High-resolution random mesh algorithms for creating a probabilistic 3D surface atlas of the human brain." *NeuroImage*, **3**(1):19–34, Feb 1996.

[WGH05] Y.L. Wang, X. Gu, K.M. Hayashi, T.F. Chan, P.M. Thompson, and S.T. Yau. "Surface Parameterization using Riemann Surface Structure." In *ICCV2005*, pp. 1061–1066, 2005.

[Woo03] R.P. Woods. "Multitracer: a java-based tool for anatomic delineation of grayscale volumetric images." *NeuroImage*, **19**:1829–1834, 2003.

[YPH06] P.A. Yushkevich, J. Piven, C. Hazlett, H. Smith, G. Smith, R. Ho, S. Ho, J. Gee, and G. Gerig. "User-guided 3D active contour segmentation of anatomical structures: significantly improved efficiency and reliability." *NeuroImage*, **31**:1116–1128, 2006.

[ZR05] J. Zhou and J.C. Rajapakse. " Segmentation of subcortical brain structures using fuzzy templates." *NeuroImage*, **28**(4):915–924, 2005.